**Astronomy
&
Astrophysics**

# APEX CO observations towards the photodissociation region of RCW 120

M. Figueira[1], A. Zavagno[2], L. Bronfman[3], D. Russeil[2], R. Finger[3], and F. Schuller[4,5]

[1] National Centre for Nuclear Research, ul. Pasteura 7, 02-093 Warszawa, Poland
  e-mail: `miguel.figueira@ncbj.gov.pl`
[2] Aix Marseille Univ., CNRS, CNES, LAM, Marseille, France
[3] Departamento de Astronomía, Universidad de Chile, Casilla 36-D Santiago, Chile
[4] Max-Planck-Institut für Radioastronomie, Auf dem Hügel 69, 53121 Bonn, Germany
[5] Leibniz-Institut für Astrophysik Potsdam (AIP), An der Sternwarte 16, 14482 Potsdam, Germany

## ABSTRACT

*Context.* The edges of ionized (H II) regions are important sites for the formation of (high-mass) stars. Indeed, at least 30% of the Galactic high-mass-star formation is observed there. The radiative and compressive impact of the H II region could induce star formation at the border following different mechanisms such as the collect and collapse or the radiation-driven implosion (RDI) models and change their properties.
*Aims.* We aim to study the properties of two zones located in the photo dissociation region (PDR) of the Galactic H II region RCW 120 and discuss them as a function of the physical conditions and young star contents found in both clumps.
*Methods.* Using the APEX telescope, we mapped two regions of size $1.5' \times 1.5'$ toward the most massive clump of RCW 120 hosting young massive sources and toward a clump showing a protrusion inside the H II region and hosting more evolved low-mass sources. The $^{12}$CO ($J = 3-2$), $^{13}$CO ($J = 3-2$) and C$^{18}$O ($J = 3-2$) lines observed, together with *Herschel* data, are used to derive the properties and dynamics of these clumps. We discuss their relation with the hosted star formation.
*Results.* Assuming local thermodynamic equilibrium, the increase of velocity dispersion and $T_{ex}$ are found toward the center of the maps, where star-formation is observed with *Herschel*. Furthermore, both regions show supersonic Mach numbers (7 and 17 in average). No substantial information has been gathered about the impact of far ultraviolet radiation on C$^{18}$O photodissociation at the edges of RCW 120. The fragmentation time needed for CC to be at work is equivalent to the dynamical age of RCW 120 and the properties of region B are in agreement with bright-rimmed clouds.
*Conclusions.* Although conclusions from this fragmentation model should be taken with caution, it strengthens the fact that, together with evidence of compression, CC might be at work at the edges of RCW 120. Additionally, the clump located at the eastern part of the PDR is a good candidate pre-existing clump where star-formation may be induced by the RDI mechanism.

**Key words.** stars: formation – ISM: bubbles – photon-dominated region – ISM: individual objects: RCW120

## 1. Introduction

High-mass stars ($M \geq 8\,M_\odot$) have a strong impact on the interstellar medium (ISM) and the formation and evolution of galaxies. Their feedback, such as the energetic radiation field and the explosion as supernovae, shapes the surrounding medium by injecting energy, momentum and metals into the ISM. (Krumholz et al. 2014; Geen et al. 2019). Therefore, while high-mass stars represent a minor part of the stellar population, the consequences of their feedback are primordial. In the study of star formation, there is one particular structure which directly relates the feedback from high-mass stars to the new generation of stars: the ionized (H II) region. That structure is created by the ionizing radiation of massive stars (Strömgren 1939), which further expands (Spitzer 1978) due to the temperature difference between the ionized gas (∼8000 K) and the surrounding medium (∼20 K). During this expansion, a layer is formed between the ionization front (IF) and the shock front (SF) that preceeds the IF during the expansion of the region into the surrounding medium. The whole structure is often called an H II bubble, even though the geometry cannot be easily assessed (Beaumont & Williams 2010; Anderson et al. 2015). Using the

WISE catalog, Anderson et al. (2014) identified 8000 of these H II regions in the Galactic plane. When the layer of material surrounding the ionizing stars is dense enough, star formation can be observed within it. This mechanism, where one or several high-mass stars are responsible for star formation, is called a triggering mechanism, and is thought to be a plausible explanation for the presence of subgroups in OB associations (Blaauw 1964; Preibisch & Zinnecker 2007). Over the years, two main models have merged to explain the formation of a new generation of stars due to the expansion of an H II region. The first is the collect and collapse (C&C, Elmegreen & Lada 1977; Whitworth et al. 1994) process, which explains the creation and fragmentation of a layer of material around an H II region, and the second is the radiation-driven implosion (RDI, Kessel-Deynet & Burkert 2003) model, where the interaction between a pre-existing, stable clump and the H II region induces star formation. Simulations of H II region expansion in a turbulent medium show the formation of pillars and cometary globules (Tremblin et al. 2012), and the expansion in a fractal medium triggers the formation of stars by combining elements from C&C and RDI (Walch et al. 2015). Several theoretical (Bertoldi 1989; Lefloch & Lazareff 1994; Miao et al. 2006) and observational studies (Urquhart et al. 2009;

Morgan et al. 2009; Fukuda et al. 2013) have analyzed the interaction between a clump and the H II region through the RDI process. This mechanism is associated with an high ionizing flux (Bisbas et al. 2011), an elongated tail, an ionized boundary layer (IBL), and 8 $\mu$m emission. Some observations have shown that several components can be observed toward bright rimmed clouds (BRCs) due to the internal dynamics caused by the interaction, although the presence of an IBL and/or 8 $\mu$m is often taken as proof of an interaction with the ionizing flux. Statistical studies using *Spitzer*, ATLASGAL, and *Herschel* showed that H II bubbles host at least 25−30% of the high-mass Galactic sources (Deharveng et al. 2010; Kendrew et al. 2012, 2016; Palmeirim et al. 2017) and dedicated studies show the same behavior (Tigé et al. 2017; Russeil et al. 2019; Xu et al. 2019). Therefore, this high percentage of young high-mass sources was mainly thought to be the result of different triggering mechanisms. However, simulations of expanding H II regions mostly showed that stars whose formation was triggered are not dominant and that spontaneously formed stars (without any help from stellar feedback) are also found at the edges of H II regions (Dale et al. 2015). Additionally, numerical simulations show that the interaction of the neutral material with the H II region could have a negative impact on star formation (Geen et al. 2015; Dale & Bonnell 2011; Dale 2017) such as lowering the star formation efficiency (SFE) compared to what is expected from observations (Geen et al. 2016; Rahner et al. 2019; Dale et al. 2012), which is therefore not in support of triggering mechanisms.

RCW 120 is a well-studied Galactic H II region because of its ovoid shape and its relatively close distance (1.34 kpc, Russeil 2003; Zavagno et al. 2007). Thanks to these advantages, this region has received a lot of attention from observers and simulations, and has been studied in several papers (Zavagno et al. 2007, 2010, 2020; Deharveng et al. 2009; Anderson et al. 2012, 2015; Tremblin et al. 2014; Kirsanova et al. 2014, 2019; Torii et al. 2015; Walch et al. 2015; Mackey et al. 2016; Figueira et al. 2017, 2018; Marsh & Whitworth 2019). Figueira et al. (2017) showed that two clumps observed at millimeter wavelength host different kinds of sources with respect to their evolutionary stage. These clumps, defined at 1.3 mm in Zavagno et al. (2007), are located in the southwest (Clump 1) and middle east (Clump 4) and are covered by regions A and B (see Fig. 1), respectively. In terms of young stellar objects (YSOs), Clump 1 hosts massive and young sources while Clump 4 hosts low-mass and more evolved sources. Considering the projected distance to the ionizing star, the expansion of the H II region should have impacted Clump 1 before Clump 4. Therefore, since high-mass star formation proceeds faster than the low-mass equivalent (Schilke 2015), we should have therefore found older sources toward Clump 1, which we did not. However, this interpretation has to be taken with caution since age gradients cannot be taken as strong evidence of triggering (Dale et al. 2013). This simple hypothesis does not take into account the mass of the cores which also plays a role in star formation timescales. Additionally, the dust distribution seen at 70 $\mu$m and the polycyclic aromatic hydrocarbon (PAH) emission at 8 $\mu$m is quite different for Clump 1 (a roughly flat layer of material) and Clump 4 (a distorted layer of material in a "V" shape). Hence, it is possible that the interaction between the H II region and the layer in the south-western and eastern parts is of a different nature. Using APEX-SheFI observations of $^{12}$CO, $^{13}$CO, and C$^{18}$O in the $J = 3−2$ transition, we studied Clumps 1 and 4 of Figueira et al. (2017) covered by regions A and B, respectively (Fig. 1).

In Sect. 2, we present the APEX observations and data reduction which are analyzed in Sect. 3. In Sect. 4, we discuss the
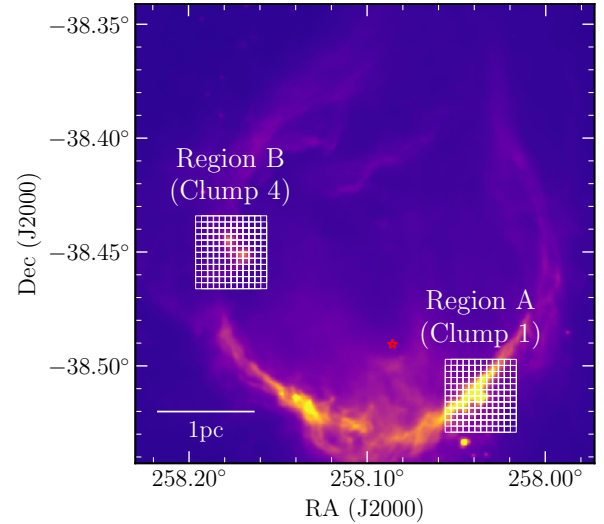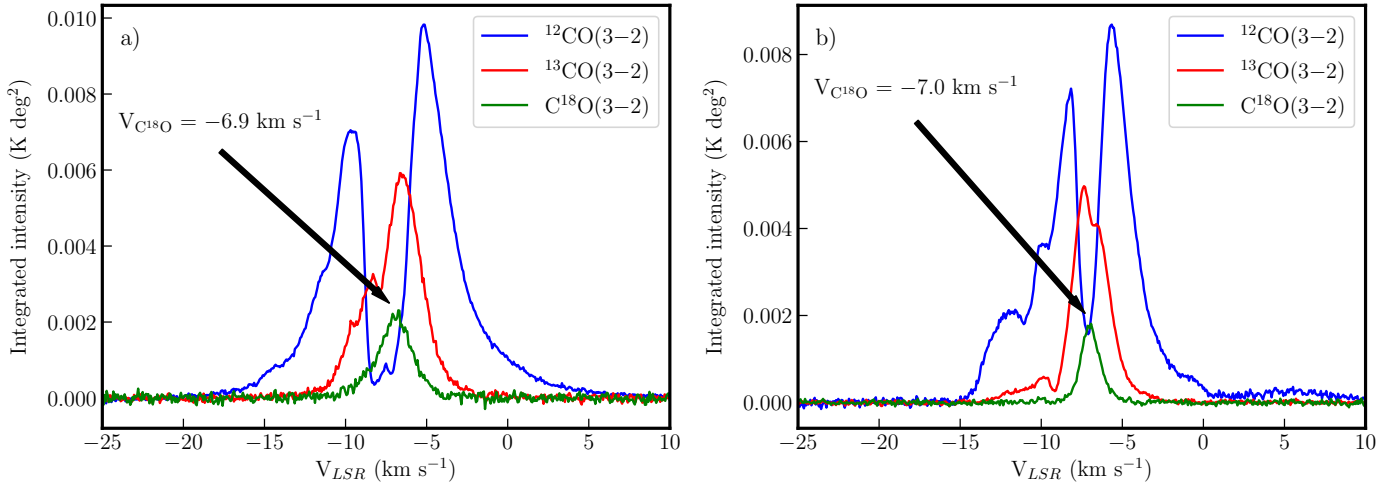
**Fig. 1.** *Herschel* 70 $\mu$m observation of RCW 120. The two grids (in white) represent the APEX observations with 121 ON observations per grid separated by half the beam for a width of 105″. The ionizing star is represented by the red star symbol.

results regarding induced star-formation and we conclude in Sect. 5.

## 2. APEX-SHeFI observations and data reduction

The $^{12}$CO (3−2), $^{13}$CO (3−2) and C$^{18}$O (3−2) molecular line transitions were observed with the Atacama Pathfinder EXperiment[1] (APEX) 12 m telescope (Güsten et al. 2006) in service mode and were carried out on October 7, 9, 11, 2016, and June 21 and September 24 and 25, 2017. The APEX Swedish Heterodyne Facility Instrument (SHeFI, Vassilev et al. 2008) band 2 receiver (267–378 GHz) was used as a front-end and the eXtended bandwidth Fast Fourier Transform Spectrometer (XFFTS, 2.5 GHz bandwidth and 32 768 spectral channels) was used as a back-end. The receiver was tuned to the $^{12}$CO (3−2) transition frequency for the $^{12}$CO (3−2) observations and to 329.960 GHz to allow the simultaneous observation of the $^{13}$CO (3−2) and C$^{18}$O (3−2) transition lines. At these frequencies, the beam size ($\theta_{\rm beam}$) and main beam efficiency ($\eta_{\rm MB}$) of the telescope are 19″.2 and 0.73, respectively. The precipitable water vapor (PWV) measuring the weather conditions during the observations ranged from 0.9 to 1.6 mm. The observations, performed with the raster mode, consist of 121 ON observations distributed as a $11 \times 11$ pixels ($\sim$105″ × 105″) mosaic map separated by half a beam with a OFF reference observed after every three ON observations in position-switching mode. The observed maps are centered on (258.03625°, −38.51319°) and (258.17625°, −38.45017°), referred as regions A and B, respectively (see Fig. 1). The integration time, excluding overheads, was 3.1 h for region A in $^{12}$CO (3−2), 3 h for region A in $^{13}$CO (3−2)/C$^{18}$O (3−2), 1.5 h for region B in $^{12}$CO (3−2), and 2.8 h for region B in $^{13}$CO (3−2)/C$^{18}$O (3−2). After the first cycle of observations (2016B), the priority was given to region B in $^{13}$CO (3−2)/C$^{18}$O (3−2) due to the low abundance of these isotopologs compared to $^{12}$CO (3−2).

**Fig. 2.** Spatially integrated intensity of $^{12}$CO (in blue), $^{13}$CO (in red), and C$^{18}$O (in green) toward regions A (a) and B (b).

Pointings and calibrations were achieved by observing NGC 6302, Mars, RT-Sco, and Saturn. The data were further reduced using the CLASS package of the GILDAS software[2]. Baselines modeled as first- to third-order polynomials were subtracted depending on the observations. The $^{13}$CO (3–2) and C$^{18}$O (3–2) observations were then tuned to their transition frequency. The *table* and *xy_map* routines were used to combine the data and create the cubes which were converted into FITS files using the *fits* routine of the VECTOR package. Finally, the cubes were resampled with a pixel size of 9.5″ to the same center and the same size in order to have uniform observations. We ended up with six spectral cubes with a resolution of 0.07 km s$^{-1}$ (76 kHz) and a rms of 0.24, 0.54, 0.89, 0.47, 0.31 and 0.37 K for region A $^{12}$CO (3–2), $^{13}$CO (3–2), and C$^{18}$O (3–2), and region B, respectively.

## 3. Analysis

### 3.1. Spatial and velocity distribution of CO (3–2), $^{13}$CO (3–2), and C$^{18}$O (3–2)

The velocity distribution of the spatially integrated emission and the velocity integrated maps for the three isotopologs and both regions are shown in Figs. 2 and 3. Due to the abundance, the integrated intensity is decreasing from $^{12}$CO to C$^{18}$O with a ratio to the $^{12}$CO peak of 1, 0.51, and 0.20 for region A, and 1, 0.51, and 0.18 for region B. The behavior of the $^{12}$CO and $^{13}$CO double peaks could either indicate the presence of two clumps or a strong self-absorption. As this is not observed in the optically thin C$^{18}$O transition, the double-peak feature is a signature of self absorption, which is clearly observed in $^{12}$CO due to high optical depth ($\tau$); it was also observed by Anderson et al. (2015) in $^{12}$CO(1–0) using MOPRA observations. The optical thickness of $^{12}$CO ($\tau_{12}$) can be estimated by comparing the intensity ratio of $^{12}$CO to $^{13}$CO to their relative abundance (Haworth et al. 2013). Assuming a $^{12}$CO and $^{13}$CO abundance of $8 \times 10^{-5}$ and $2.7 \times 10^{-6}$, respectively (Magnani et al. 1988; Pineda et al. 2008), the abundance ratio is approximately 30, which is much higher than the average line intensity ratio of 2.4, indicating a high optical depth for $^{12}$CO. The $^{13}$CO presents some self-absorption features, especially toward region A, in agreement with the fact that clump 1 is the densest of RCW 120.

The Gaussian fit of C$^{18}$O indicates that this molecular line is centered at −6.9 km s$^{-1}$ for region A and −7.0 km s$^{-1}$ for region B, respectively. As RCW 120 has a $V_{LSR}$ of −7 to −8 km s$^{-1}$, these two emissions are associated with its photo dissociation region (PDR).

Two features are observed in the southeast part of region A. A small peak is detected only in $^{12}$CO at approximately −15 km s$^{-1}$ (white pixels on Fig. A.1) with a $T_{MB}$ of less than 5 K. This feature may be too weak to be detected in other isotopologs and could be due to line-of-sight contamination as it does not appear to be related to the PDR or the ionized region. The other feature can be seen at −12.5 km s$^{-1}$ and located in the northwest part of the region where the ionized gas is; it is weaker toward the PDR. Its location on the blue side of the spectrum may be evidence that the $^{12}$CO gas is moving toward us due to the ionization pressure. These two features can only be weakly seen on the spatially averaged profile (Fig. 2) at approximately −14.5 and −12 km s$^{-1}$. Toward region B, we note the non-Gaussian profile with asymmetry on the blue part. In addition to the main component, three others can be seen at approximately −12, −10, and −1 km s$^{-1}$. These are discussed in Sect. 3.6.

We constructed the mean velocity and velocity dispersion maps[3], also known as first- and second-moment maps, of the $^{13}$CO and C$^{18}$O and a clip at $3\sigma$ (Fig. 4). The mean velocity of the $^{13}$CO and C$^{18}$O in region A ranges from −8.3 to −5.5 km s$^{-1}$ with an average of −7 km s$^{-1}$. While a range of different velocities is observed, the interval is too small and no clear gradients or particular features are observed. The average velocity dispersion is 0.7 km s$^{-1}$ for C$^{18}$O, which is in good agreement with the velocity dispersion of 0.8 km s$^{-1}$ found towards the PDR of RCW 120 with MOPRA CO (1–0) data (Anderson et al. 2015). Our observations seem to be in agreement for $^{13}$CO with an average of 1.4 km s$^{-1}$ (see their Fig. 9). On the velocity dispersion maps, the center of region A stands out with a velocity dispersion of 2.6 and 1.1 km s$^{-1}$ for $^{13}$CO and C$^{18}$O, respectively, and shows the increase of line width through turbulence and thermal contributions from the Class 0 *Herschel* source 2.

In region B, the mean velocity of the $^{13}$CO and C$^{18}$O ranges from −7.2 to −6.6 km s$^{-1}$ with an equal average of −6.9 km s$^{-1}$. In $^{13}$CO, the mean velocity does not seem to

---

[2] http://www.iram.fr/IRAMFR/GILDAS

[3] The mean velocity and velocity dispersion are computed following $M_1 = \int T_{MB} V dV / \int T_{MB} dV$ and $M_2 = \int T_{MB}(V - M_1) dV / \int T_{MB} dV$.
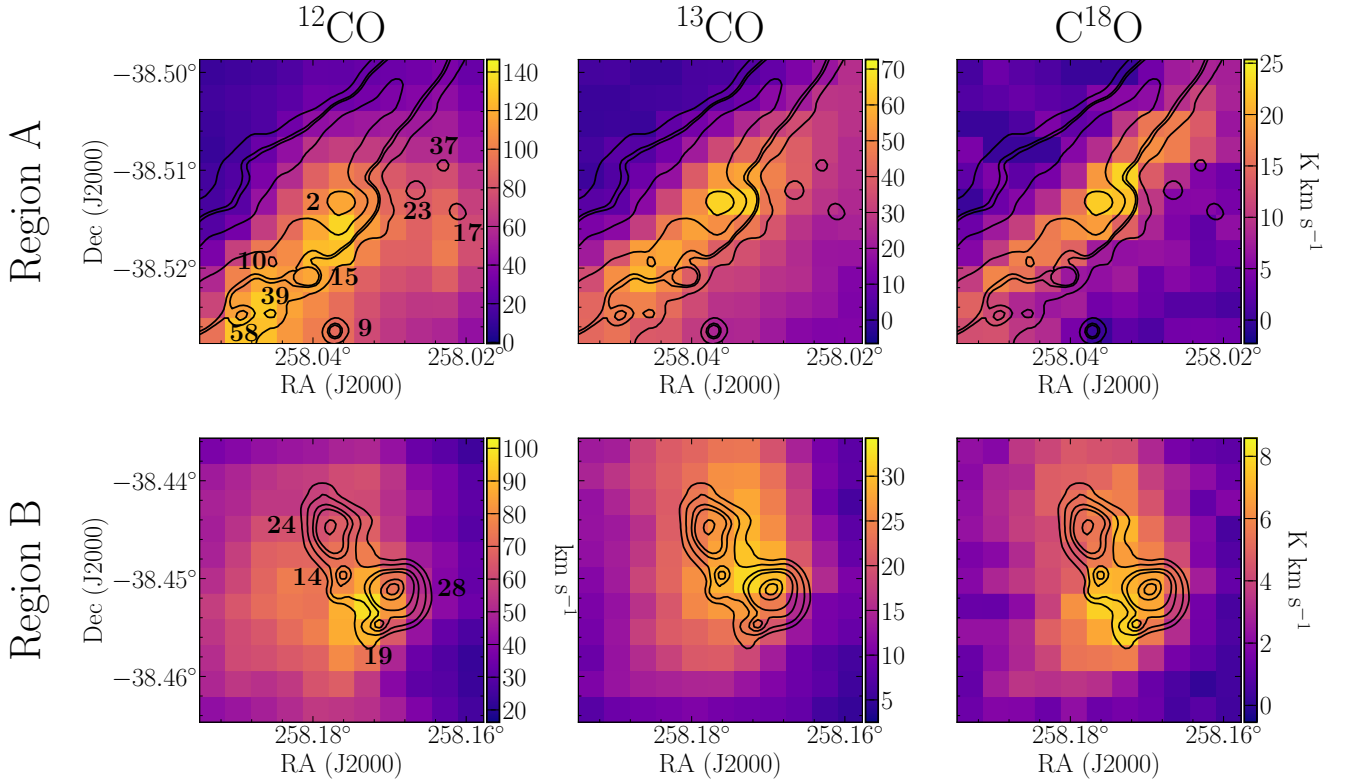
**Fig. 3.** Velocity integrated intensity of the $^{12}$CO (3−2) (*first column*), $^{13}$CO (3−2) (*second column*), and C$^{18}$O (3−2) (*third column*) for regions A (*top*) and B (*bottom*). The velocity range used for integration is $-20.1 < V_{LSR} < 8.2$ km s$^{-1}$, $-15.0 < V_{LSR} < 3.1$ km s$^{-1}$, and $-12.0 < V_{LSR} < -2.3$ km s$^{-1}$ for $^{12}$CO (3−2), $^{13}$CO (3−2), and C$^{18}$O (3−2), respectively. Contours represent the emission at 70 $\mu$m from *Herschel* and the cores (labels are slightly shifted from the true position of the cores) which were extracted in Figueira et al. (2017).
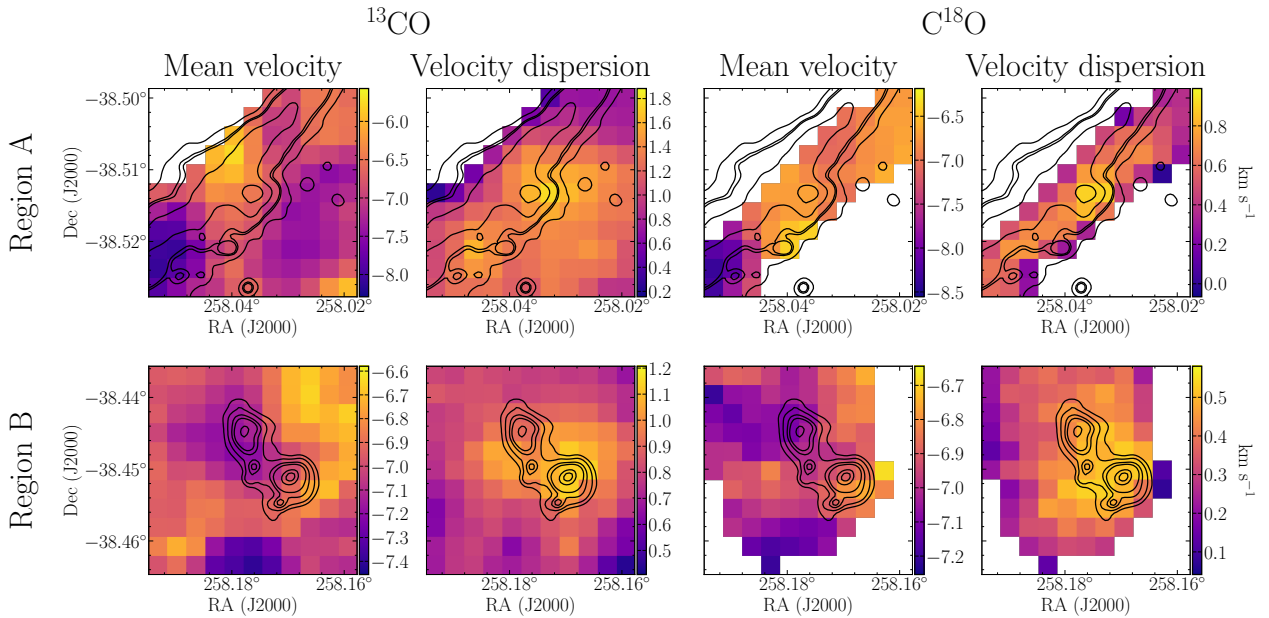


**Fig. 4.** Mean velocity and velocity dispersion maps of $^{13}$CO (3−2) (*first and second columns*) and C$^{18}$O (3−2) (*third and fourth columns*) towards regions A (*top*) and B (*bottom*). The integration velocity and contour levels are the same as in Fig. 3.

be distributed randomly in the map with lower mean velocity toward the H II region and higher toward the clump, but as for region A, the range of velocity is too small for any meaningful conclusions to be made. Higher spatial and spectral resolution observations are needed to study gas motions in these two regions. The velocity dispersions of 0.8 and 0.4 km s$^{-1}$

are also consistent, on average, with the MOPRA observations, and show larger values where the evolved low-mass sources are located.

Due to the temperature difference between the most massive core of RCW 120 (labeled as core 2; see Figueira et al. 2017 and Fig. 3) with $T_{dust} = 20.3$ K and the YSOs in region B with
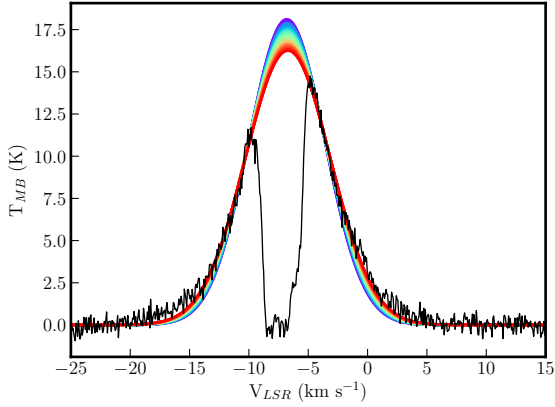
**Fig. 5.** $^{12}$CO spectrum in region A. The purple curve corresponds to the fit using the upper part of the shoulders while the red curve is obtained using the whole spectrum except the self-absorption feature.

$T_{\mathrm{dust}} = 34.1$ K, turbulence toward region A should be higher in order to explain the higher velocity dispersion. This is in agreement with the high-mass star formation occurring in this core (Figueira et al. 2018) compared to the low-mass YSOs present in region B.

### 3.2. Self-absorption correction

The self-absorption feature seen in $^{12}$CO and $^{13}$CO (see Fig. 2) is responsible for the intensity loss at the $V_{\mathrm{LSR}}$ of the region ($-7$ km s$^{-1}$) resulting in a lower $T_{\mathrm{MB}}$ than expected. To correct the spectra for self-absorption, we performed iterative Gaussian fittings using the shoulder of the profile. We began with the upper part of the profile shoulders and iteratively performed fittings by increasing their length until reaching the end of the profile. Secondary peaks were removed during the fitting. As seen in Fig. 5, when using a smaller length (bluer color), the peak tends to be higher compared to the length of the larger shoulders (redder color). The uncertainty on the peak value was computed as the standard deviation of the different peak values while it was computed as the $1\sigma$ uncertainty if no self-absorption was observed. Hence, each spectrum could be fitted with a single Gaussian, and a peak main brightness temperature could be derived for each of them ($T_{\mathrm{MB}}^{12}$, $T_{\mathrm{MB}}^{13}$ and $T_{\mathrm{MB}}^{18}$). As self-absorption decreases, either going from $^{12}$CO to C$^{18}$O or from region A to region B where CO is less abundant, the uncertainties on $T_{\mathrm{MB}}$ decrease. Toward region B, 100 and 34% of the spectra are corrected for self-absorption while this is 88 and 23% for region A, for $^{12}$CO and $^{13}$CO. In the following, all the peak values are corrected for self-absorption.

### 3.3. Physical properties of the clumps

The solution of the radiative transfer equation can be used to derive several physical properties of the clumps such as the excitation temperature $T_{\mathrm{ex}}$, the optical depth $\tau$, and the column density $N$. Assuming that the medium is uniform, the background-subtracted solution of the radiative transfer equation can be written explicitly using the Planck law and rearranged to obtain $T_{\mathrm{ex}}$ as a function of $T_{\mathrm{MB}}$, the CMB temperature $T_{\mathrm{CMB}}$, and $\tau$ (Rohlfs & Wilson 1996; Haworth et al. 2013):

$$T_{\mathrm{ex}} = T_\nu \left[ \ln \left( 1 + T_\nu \frac{1 - \mathrm{e}^{-\tau}}{T_{\mathrm{MB}} + T_\nu (1 - \mathrm{e}^{-\tau}) \mathrm{e}^{\frac{-T_\nu}{T_{\mathrm{CMB}}}}} \right) \right]^{-1}, \quad (1)$$

**Table 1.** Parameters used to compute $T_{\mathrm{ex}}$, $\tau$, and $N$.

| CO (3−2) $J_l = 2$ | $\nu$ (GHz) | $T_\nu$ (K) | $\exp(-T_\nu/T_{\mathrm{CMB}})$ | B (GHz) |
|---|---|---|---|---|
| $^{12}$CO | 345.795 | 16.6 | 0.0022 | 57.635 |
| $^{13}$CO | 330.587 | 15.9 | 0.0029 | 55.101 |
| C$^{18}$O | 329.330 | 15.8 | 0.0030 | 54.891 |

where $T_\nu = h\nu/k_{\mathrm{B}}$, $k_{\mathrm{B}}$ is the Boltzmann constant, $h$ is the Planck constant, and $\nu$ is the frequency transition of the line considered. The parameters of Eq. (1) can be found in Table 1 for the $J = 3-2$ transition. As shown in Sect. 3.1, $^{12}$CO is optically thick and so $T_{\mathrm{ex}}$ can be simplified considering $\tau \rightarrow \infty$.

Toward region A, $T_{\mathrm{ex}}$ is minimal inside the H II region (6.7 K) where the $^{12}$CO is less abundant, and increases along the PDR where star formation is observed, with the highest value (38.3 K) being found towards the center where the *Herschel* source 2 is located; the average over the whole region is 22.8 K. Toward region B, the excitation temperature is also minimal inside the H II region (10.5 K) and increases up to 40.9 K towards the center of the clump where evolved low-mass stars are observed; the average over region B is 20.7 K. These values agree with $T_{\mathrm{ex}} = 23.4$ K from Anderson et al. (2015) and are similar to those toward the mid-infrared bubble S 44 (Kohno et al. 2018) where ranges of $8-13$ K and $8-25$ K were found. The locations of the $T_{\mathrm{ex}}$ high values (see Fig. 6) are associated with the *Herschel* sources which, together with the far ultraviolet (FUV) radiation from the H II region, are another important source of heating.

By inverting Eq. (1) and assuming local thermodynamical equilibrium (LTE), $\tau_{13}$ and $\tau_{18}$ can be computed through Eq. (2):

$$\tau = -\ln \left[ 1 - \frac{T_{\mathrm{MB}}}{T_\nu \left( \frac{1}{\mathrm{e}^{T_\nu/T_{\mathrm{ex}}} - 1} - \mathrm{e}^{-T_\nu/T_{\mathrm{CMB}}} \right)} \right]. \quad (2)$$

Towards region A, the optical depth of $^{13}$CO and C$^{18}$O follows the same behavior as in $T_{\mathrm{ex}}$ with low values away from the PDR (around 0.2 and 0.1 inside the H II region) and higher values (up to 2.3 and 0.7) towards the PDR. On average, $^{13}$CO has a larger optical depth compared to C$^{18}$O, the former being moderately thick along the PDR and the latter optically thin everywhere. In region B, the values of $\tau_{13}$ and $\tau_{18}$ range from 0.2 and 0.1 inside the H II region to 2.7 and 0.4, respectively, with a similar average compared to region A. We note that the highest values of $\tau$ are always found at the edges of the map and we cannot exclude that the resampling process lowered the quality of the border of the map. If these high values are excluded, $^{13}$CO is moderately thick with $\tau_{13}$ reaching values up to 1.5.

By studying a sample of bright rim clouds (BRCs), Morgan et al. (2009) showed that $T_{\mathrm{ex}}^{18}$ can be significantly different from $T_{\mathrm{ex}}^{12}$ because C$^{18}$O probes the interior of the clump due to its low optical thickness compared to $^{12}$CO which is mostly representative of the surface of the clump (Takekoshi et al. 2019). Using Eq. (1), an estimation of $T_{\mathrm{ex}}$ for C$^{18}$O can be computed using the average $\tau_{18}$ found with Eq. (2). To make a comparison with $T_{\mathrm{ex}}^{12}$, we only take into account the $^{12}$CO pixels where C$^{18}$O is detected. On average, $T_{\mathrm{ex}}^{12}$ is higher than $T_{\mathrm{ex}}^{18}$ as observed but with a lower temperature difference ($2-4$ K) than in Morgan et al. (2009). Stars and protostars located inside regions A and B could explain this rise of $T_{\mathrm{ex}}^{18}$ as clumps are not quiescent.
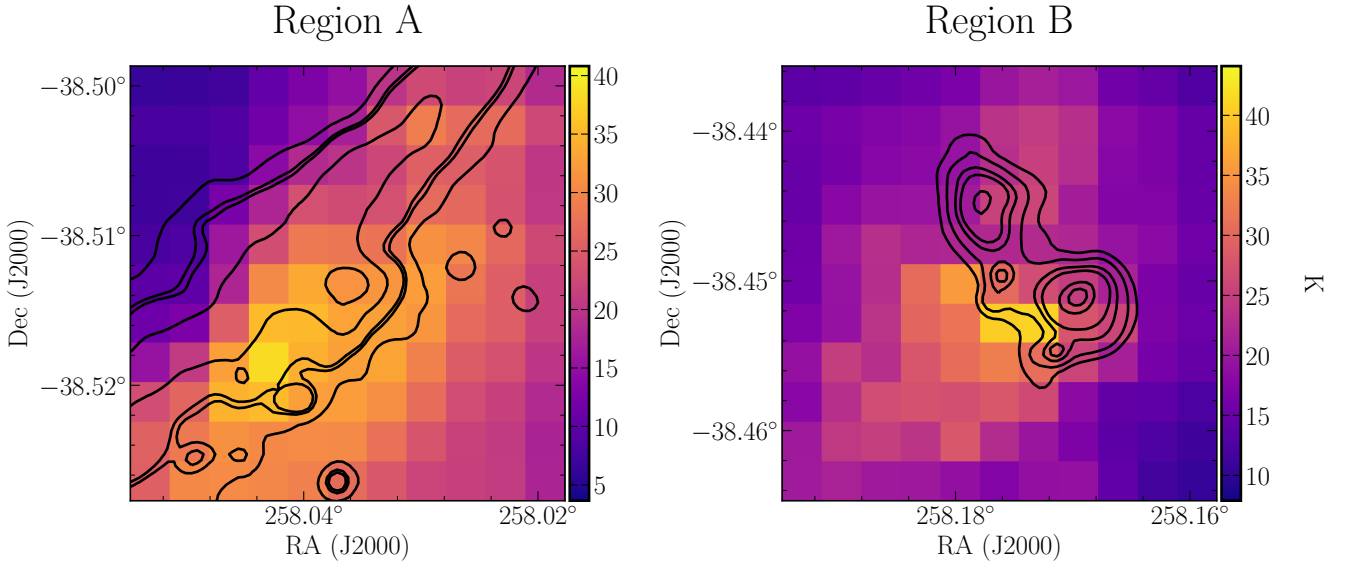
Region A

Region B



**Fig. 6.** $T_{ex}$ toward regions A (*left*) and B (*right*) obtained using Eq. (1).

The column density of $^{13}$CO and C$^{18}$O (see Fig. 7) can be obtained with:

$$N = \left(\frac{3k_{\mathrm{B}}}{8\pi^3 B\mu^2}\right)\left(\frac{e^{hBJ_l(J_l+1)/k_{\mathrm{B}}T_{ex}}}{J_l+1}\right)\left(\frac{T_{ex}+hB/3k_{\mathrm{B}}}{1-e^{h\nu/k_{\mathrm{B}}T_{ex}}}\right)\int \tau \mathrm{d}\upsilon, \qquad (3)$$

$$\int \tau \mathrm{d}\upsilon = \frac{1}{T_\nu\left(\frac{1}{e^{T_\nu/T_{ex}}-1}-e^{-T_\nu/T_{\mathrm{CMB}}}\right)}\frac{\tau}{1-e^{-\tau}}\int T_{\mathrm{MB}}\mathrm{d}\upsilon. \qquad (4)$$

Towards region A, N($^{13}$CO) follows the PDR of RCW 120 with a maximum of $5.5 \times 10^{16}$ cm$^{-2}$ found towards the most massive core of the region. The N(C$^{18}$O) distribution also follows the PDR but with less variation, a maximum of $1.4 \times 10^{16}$ cm$^{-2}$ toward the massive core, and a decrease away from it. Towards region B, the N($^{13}$CO) and N(C$^{18}$O) distributions are well correlated with the dust continuum emission with values toward the center of $2.7 \times 10^{16}$ and $4.1 \times 10^{15}$ cm$^{-2}$, respectively. Since the column density calculation depends on $\tau$, a similar issue arises toward the edge of the map, mainly seen for N($^{13}$CO) in both regions. The global values of column density found toward this region are in agreement with other star-forming regions (Shimajiri et al. 2014; Paron et al. 2018; Vazzano et al. 2019). Inside the H II region, no $^{13}$CO (3−2) and C$^{18}$O (3−2) are detected. Given the rms of these observations, we derive an upper limit for the column density of $1.5 \times 10^{15}$ cm$^{-2}$ and $7.5 \times 10^{13}$ cm$^{-2}$ for $^{13}$CO and C$^{18}$O, respectively. The values of the physical parameters discussed above are listed in Table 2.

### 3.4. Outflows toward RCW 120

#### 3.4.1. Extraction of the wings

During the phase of high-mass star formation, one of the solutions proposed to overcome the radiation pressure problem (Wolfire & Cassinelli 1987) was the growth of the star via an accretion disk (Jijina & Adams 1996) such as in the formation of low-mass stars (Coffey et al. 2008). For the angular momentum to be conserved, high-mass stars formed by disk accretion must radiate this excess of momentum via outflows. Observations show that high-mass star formation is associated with outflows (Arce et al. 2007; Maud et al. 2015; McLeod et al. 2018). Since

high-mass stars release more momentum and energy, and their outflows spawn a larger distance, high-mass star outflows are more easily detectable compared to those from low-mass stars. During high-mass star formation, outflows develop during the hot-core stage preceding the UCH II phase, which is also associated with the 6.67 GHz class II methanol maser (Caswell 2013). The detection of outflows is mostly done through the identification of wings on spectral profiles but other indirect tracers of outflows exist such as SiO.

Toward region A, source 2 observed with *Herschel* is a massive source where high-mass star formation is observed through the hot core phase (Figueira et al. 2018). Several molecular transitions (MALT90 survey) such as tracers of hot core (CH$_3$CN and HC$_3$N) as well as a tracer of shock and outflow (SiO) are observed toward source 2, strongly indicating that an outflow is present. The profile is broad (Kirsanova et al. 2019) and synonymous of the dynamics toward this core. SiO is also detected toward source 39, but as it is placed at the edge of the map, we did not extract the outflow because the edges are problematic due to the resampling process; however, it may contaminate the properties of the outflow at the location of source 2. Toward region B where low-mass sources are observed, no wings or outflow tracers are detected. Sources are classified as Class I, II, or Ae/Be stars (Deharveng et al. 2009; Figueira et al. 2017) and due to the more evolved stage of these sources, the outflows, if any, should be weaker compared to region A.

To extract the outflow wings from our spectra, we employed the method of de Villiers et al. (2014) used in the framework of methanol masers as a counterpart of the hot core stage, which was also used in Yang et al. (2018) toward ATLASGAL clumps. The procedure to extract the wings of the spectrum is visually explained in Fig. 8 and the basic idea is to retrieve the part of the $^{13}$CO spectrum that is broader than the C$^{18}$O spectrum. Firstly, the C$^{18}$O spectrum is scaled to the peak of the $^{13}$CO spectrum and is then fitted with a Gaussian. In order to remove high-velocity features (van der Walt et al. 2007) and correctly fit the spectrum peak, we first performed a fit of the whole spectrum and we iteratively fitted the spectrum by reducing the length of the shoulders pixel to pixel (see Fig. 8 left). This modeled, scaled C$^{18}$O spectrum is then subtracted from the observed $^{13}$CO spectrum to obtain the $^{13}$CO residuals. The blue and red wings are

## Region A

### $^{13}$CO  C$^{18}$O

### Region B

### $^{13}$CO  C$^{18}$O
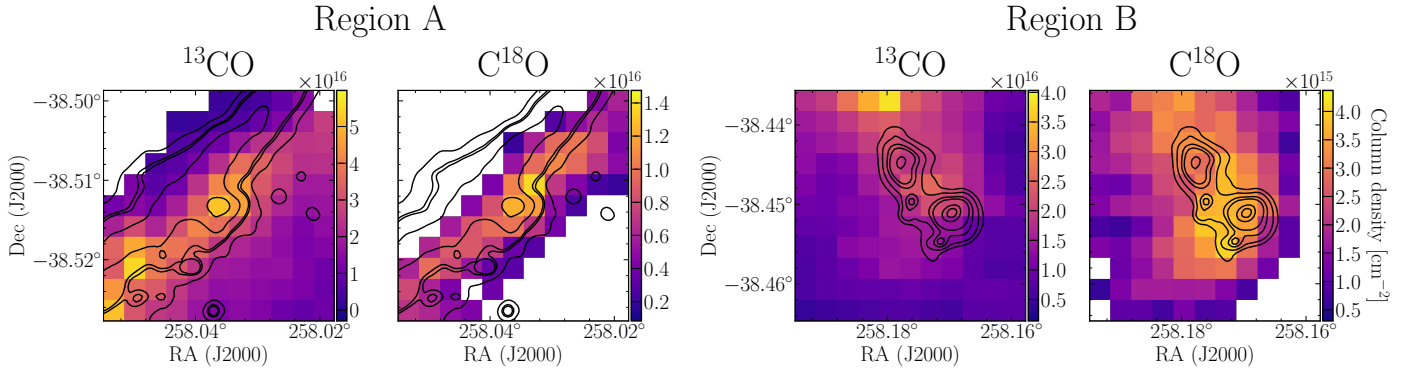


**Fig. 7.** Column density of $^{13}$CO and C$^{18}$O for region A (*first and second columns*) and region B (*third and fourth columns*).

**Table 2.** $T_{\rm ex}$ from $^{12}$CO and C$^{18}$O, and optical depth and column density of $^{13}$CO and C$^{18}$O.

|  |  | $T_{\rm ex}^{12}$ (K) | $T_{\rm ex}^{18}$ (K) | $\tau_{13}^{\rm LTE}$ | $\tau_{18}^{\rm LTE}$ | $N(^{13}{\rm CO})^{\rm LTE}$ (cm$^{-2}$) | $N({\rm C}^{18}{\rm O})^{\rm LTE}$ (cm$^{-2}$) |
|---|---|---|---|---|---|---|---|
| | Minimum | 6.7 (18.7) | 14.8 | 0.2 | 0.1 | $2.1 \times 10^{15}$ | $1.9 \times 10^{14}$ |
| Region A | Maximum | 38.3 (38.3) | 39.1 | 2.3 | 0.7 | $5.5 \times 10^{16}$ | $1.4 \times 10^{16}$ |
| | Mean | 22.8 (28.3) | 24.8 | 0.7 | 0.3 | $2.2 \times 10^{16}$ | $6.5 \times 10^{15}$ |
| | Minimum | 10.5 (13.9) | 9.7 | 0.2 | 0.1 | $4.4 \times 10^{15}$ | $6.2 \times 10^{14}$ |
| Region B | Maximum | 40.9 (40.9) | 34.7 | 2.7 | 0.4 | $3.8 \times 10^{16}$ | $4.1 \times 10^{15}$ |
| | Mean | 20.7 (21.8) | 19.9 | 0.7 | 0.2 | $1.3 \times 10^{16}$ | $2.1 \times 10^{15}$ |

defined as the part of the $^{13}$CO spectrum corresponding to the $^{13}$CO residuals above $3\sigma$ and below the two maxima of the residuals, or, in other words, the part of the $^{13}$CO spectrum which is broader than the scaled C$^{18}$O spectrum (see Fig. 8 right). Toward region A, the $^{13}$CO spectrum was corrected for self-absorption, as explained in Sect. 3.2. When Gaussian fitting was performed, we first convolved the signal using a one-dimensional box of five pixels in order to remove the fluctuations. By visual inspection, we checked that this process does not smooth the particular features of our spectra (self-absorption, wings, secondary peaks).

The $^{13}$CO spectrum was then integrated in the velocity windows defined by the wings. These wings are presented on Fig. 9 where the lowest contour is visually chosen as the one enclosing the wings on the integrated map. As it is difficult to differentiate between the background and the emission wings, this leads to a higher uncertainty when deriving the parameters of the outflow as they depend on the mass of the wings, which itself depends on the lowest contour used.

### 3.4.2. Outflow properties

The mass of the blue and red wings represented in Figs. 8 and 9 is computed by integrating the areas of the lobes on the N($^{13}$CO) map integrated over the velocity ranges of the wings. Using the abundance of $^{13}$CO relative to H$_2$ from *Herschel* observations, N($^{13}$CO) is converted into a mass. The total mass of the outflow is obtained by summing the contribution of the blue and red lobes. An estimation of the outflow momentum and energy were obtained by summing each contribution from the velocity channels corresponding to the blue and red wings. The dynamical timescale $t_{\rm D}$, the mass-loss rate $\dot{M}_{\rm out}$, the mechanical force $F_{\rm m}$, and luminosity $L_{\rm m}$ of the outflow were then computed (see Eqs. (4)–(9) in Yang et al. 2018).

The properties of the outflows in region A can be found in Table 3. When computing the properties of outflows, we have to account for several parameters which increase their uncertainty (see Sect. 4.3 of de Villiers et al. 2014). One of the most severe is the inclination of the outflow with respect to the line of sight. If this property is unknown, the corrections are either not done or are applied assuming a uniform distribution in the sky ($\theta = 57.3°$). In this paper, we do not correct for the inclination but the reader can refer to Table 4 of de Villiers et al. (2014) and apply the correction factors in case of comparison with other works. The values of the massive core 2 outflow (376 $M_\odot$, 856 $L_\odot$ Figueira et al. 2018) are in relatively good agreement with the general values for massive star forming (MSF) clumps derived by Yang et al. (2018) with a sample of 153 ATLASGAL clumps and by de Villiers et al. (2014) from methanol-maser-associated outflows. Since the mass of the wings derived from N(H$_2$) might be overestimated, we account for an uncertainty on the outflow properties of between a factor of two and three greater than those in de Villiers et al. (2014) and Yang et al. (2018).

### 3.5. Estimation of the Mach number

The turbulence in molecular clouds is an important parameter to take into account in star formation as it can counteract the gravity during the gravitational collapse of a core. The solenoidal and compressive modes of turbulence have different impacts on star-formation, where the latter is thought to be associated with a higher star formation efficiency (SFE; Federrath & Klessen 2012). The goal here is not to derive the ratio of solenoidal to compressive modes as was done in Orkisz et al. (2017) but rather to obtain an estimation of the Mach number $M$. The thermal line width of the line $c_{\rm T}$ is defined by $\sqrt{k_{\rm B}T/\mu m_{\rm H}}$ where $T$ is taken to be the maximal temperature between $T_{\rm ex}$ (from $^{12}$CO) and $T_{\rm dust}$ (from *Herschel* observations) as recommended by
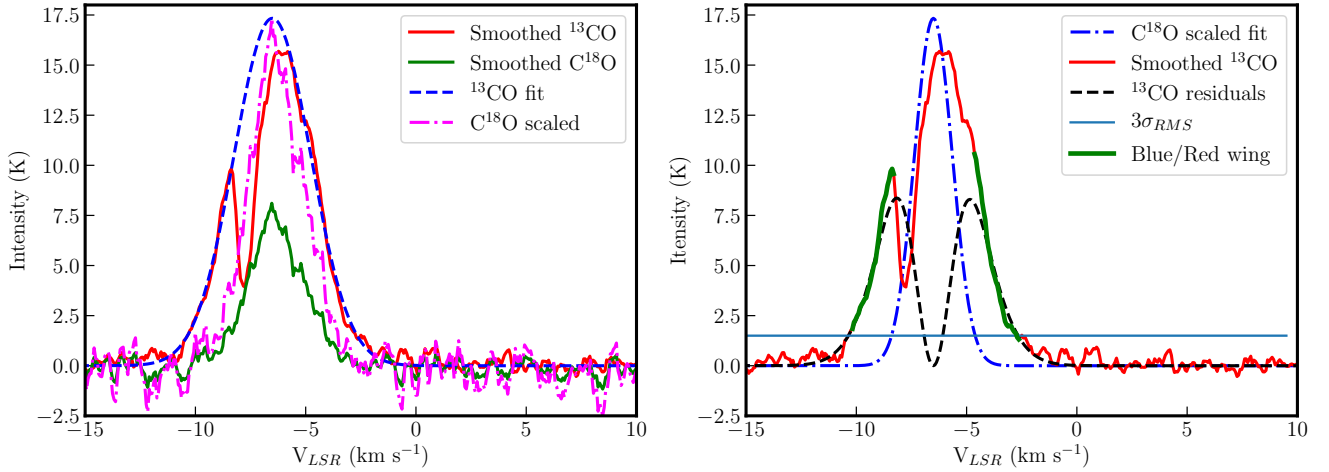
**Fig. 8.** Application of the method described in Sect. 3.4 to source 2 of region A. *Left*: $^{13}$CO and C$^{18}$O spectra convolved with a 1D box of 5 pixels (continuous red and green lines), the Gaussian fit of the $^{13}$CO to correct for the self-absorption (dashed blue line), and the C$^{18}$O spectrum scaled to the peak of the $^{13}$CO Gaussian fit (dashed-point magenta line). *Right*: Gaussian fit to the scaled C$^{18}$O spectrum (dashed-point blue line), $^{13}$CO residual (dashed black line) resulting from the subtraction of the scaled C$^{18}$O Gaussian from the $^{13}$CO Gaussian, and the blue and red wings (green line).
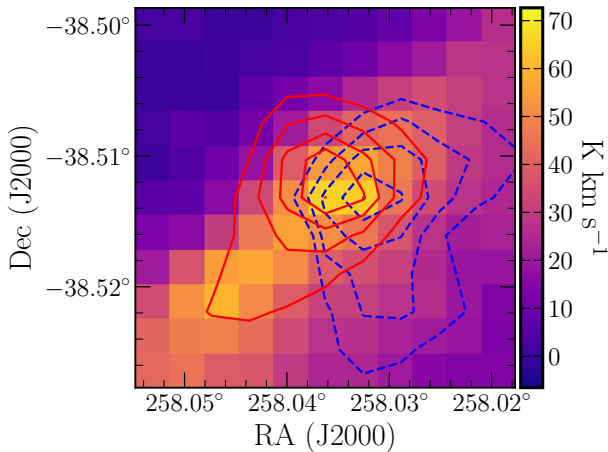


**Fig. 9.** Outflow contours in region A for the red and blue wings (continuous red and dashed blue contours) overlaid on the $^{13}$CO (3−2) velocity integrated intensity image.

Orkisz et al. (2017). The nonthermal component of the line width is $\sigma_{\rm NT} = \sqrt{\sigma^2 - \sigma_{\rm T}^2}$ where $\sigma$ is the dispersion of the $^{13}$CO spectra related to the FWHM by $\sigma = FWHM/\sqrt{8\ln2}$. The Mach number is defined as $M = \sigma_{\rm NT}/c_{\rm S}$, where $c_{\rm S}$ is the sound speed. The median for regions A and B is 17 and 7, respectively. In Orkisz et al. (2017), $M$ increases to values higher than 20 towards the regions where the FWHM of the $^{13}$CO is high. However, as their observations do not only focus on the star-forming parts of Orion-B but on the whole region, the median $M$ decreases to 6. In our case, observations were centered on two star-forming regions which explains the higher $M$. Such high values of $M$ have been observed for instance toward Orion A (González Lobos & Stutz 2019), GMF38a (Wu et al. 2018), and quiescent 70 $\mu$m clumps (Traficante et al. 2018).

### 3.6. Impact of the H II region on the layer

Contrary to the rest of the ring, region B is the most intriguing due to its particular morphology. As seen on Fig. 10, the 8 $\mu$m

**Table 3.** Outflow properties.

| Parameters | Core 2 |
|---|---|
| $M_{\rm out}$ ($M_\odot$) | 116 |
| $p$ ($M_\odot$ km s$^{-1}$) | 281 |
| $E$ (J) | $7.3 \times 10^{38}$ |
| $t_{\rm D}$ (yr) | $1.6 \times 10^4$ |
| $\dot{M}_{\rm out}$ ($M_\odot$ yr$^{-1}$) | $7 \times 10^{-3}$ |
| $F_{\rm m}$ ($M_\odot$ km s$^{-1}$ yr$^{-1}$) | $1.7 \times 10^{-2}$ |
| $L_{\rm m}$ ($L_\odot$) | 3.7 |

observation shows a distorted emission as if a clump was pre-existing. This fact is particularly clearly seen when following the distribution of 8 $\mu$m emission traced by the dashed red circle in Fig. 10 where the clump and the bow structures are clearly seen inside the circle. The bow would be the result of lower density wings which would have been swept up by the radiation compared to the central overdensity of the clump. The radio emission at 843 MHz from the Sydney University Molonglo Sky Survey (SUMSS), seen in black contours, also shows a distortion around the clump of region B, indicating interplay between the ionizing radiation and the clump. In the northern part of the clump, where the SUMSS emission is present, it can also be noted that an 8 $\mu$m arc is present, touching the last contour. The tails can also be observed on the velocity integrated image of C$^{18}$O (Fig. 3) but this is not really clear as the resolution of the CO observations (∼18.2′′) is lower than *Spitzer* 8 $\mu$m and *Herschel* 70 $\mu$m observations.

Using radio continuum emission, the photon flux $\Phi$ impacting the clump of region B and the corresponding electron density $n_{\rm e}$ can be computed with the following equation (Lefloch et al. 1997; Thompson et al. 2004):

$$\Phi = 1.24 \times 10^{10} \times \left[\frac{S_\nu}{\rm mJy}\right] \times \left[\frac{T_{\rm e}}{\rm K}\right]^{0.35} \times \left[\frac{\nu}{\rm GHz}\right]^{0.1} \times \left[\frac{\theta}{''}\right]^{-2}, \quad (5)$$

$$n_{\rm e} = 122.21 \times \left(\frac{S_\nu T_{\rm e}^{0.35} \nu^{0.1}}{\theta^2}\right)^{\frac{1}{2}} \times \left[\frac{\eta R_{\rm c}}{\rm pc}\right]^{-\frac{1}{2}}. \quad (6)$$
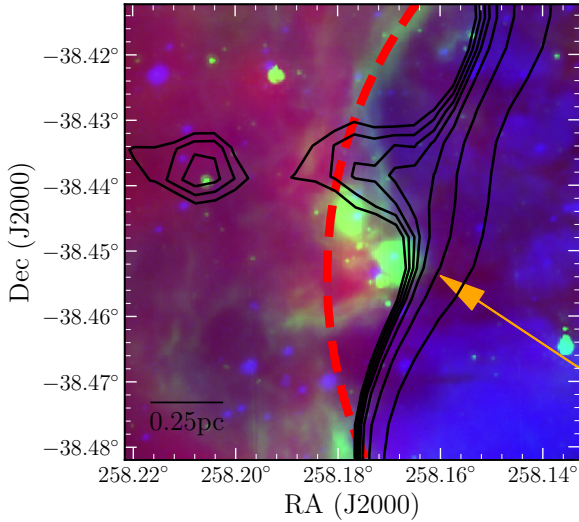
**Fig. 10.** Observation of region B from *Spitzer* at 8 μm, where the red dashed line represents the circle which follows the 8 μm emission, the black contours represent the free-free emission from SUMSS (contours from 0.01 to 0.04 Jy beam$^{-1}$), and the orange arrow indicates the direction of the ionizing radiation. The clump with the tails is inside the circle.

The electron temperature inside the H II region computed from Balser et al. (2011) gives $T_e = 8100$ K, in agreement with the range of $T_e$ ($7 \times 10^3$ to $10^4$ K) used in other works (Anderson et al. 2015). In Eqs. (5) and (6), $\theta$ is the angular diameter where the flux is integrated, $R_c$ is the radius of clump impacted by the radiation, and $\eta$ is the fraction of the clump that is photoionized. At 835 MHz, the flux is equal to 7 Jy in $\theta = 506''$, $R_c$ is taken to be ~0.18 pc, and we assume the general value $\eta = 0.2$ (Bertoldi 1989). The corresponding $\Phi$ at the interface between the H II region is equal to $(8 \pm 1) \times 10^9$ cm$^{-2}$ s$^{-1}$. The value of the electron density $n_e$ at the edge of the clump is ~$(510 \pm 30)$ cm$^{-3}$ which is far above the electron density value needed to form an ionized boundary layer (IBL). Uncertainties were estimated using $T_e = 7000-10\,000$ K and an uncertainty of 5% for the flux (Murphy et al. 2007). We note that the emission at 843 MHz could be optically thick and underestimated. Using the measurement from Caswell & Haynes (1987) at 5 GHz for the whole region and equal to 8.3 Jy, $\Phi$ and $n_e$ increase to $1 \times 10^{10}$ cm$^{-2}$ s$^{-1}$ and 600 cm$^{-3}$, respectively.

To understand if the pressure of the H II region could have pushed and compressed the clump of region B, we computed the pressure at the edge of the clump due to ionization, $P_{ion}$, and the internal pressure of the clump, $P_{clump}$. The ionization pressure of an H II region is estimated with $P_{ion} = 2n_e T_e$ (Urquhart et al. 2004). The ionization pressure $P_{ion}/k_B$ is found to be $(8 \pm 2) \times 10^6$ K cm$^{-3}$. This value is similar to the one found toward the horsehead nebula (Ward-Thompson et al. 2006) with an O9.5 star at a distance of ~3.5 pc. The pressure of the clump is computed following $P_{clump} = \rho_{clump} \sigma^2$ where $\rho_{clump}$ is the clump density and $\sigma$ (~$1 \pm 0.2$ km s$^{-1}$) is the velocity dispersion of $^{13}$CO toward the clump. The pressure $P_{clump}/k_B$ is around $(8 \pm 3) \times 10^6$ K cm$^{-3}$.

If the clump was pre-existent without star-formation, the dispersion would mainly be thermal with $\sigma_{th} \sim 0.2$ (at 10 K), giving an upper limit of $1 \times 10^6$ K cm$^{-3}$ for $P_{clump}/k_B$. In this initial configuration, the clump of region B is firstly compressed by the H II region pressure causing the gravitational collapse of the clump, the formation of stars, and the increase of $P_{clump}$ through the increase of turbulence and temperature. When $P_{clump} \sim P_{ion}$, the highest density part of the clump stops to be compressed but the less dense part continues to be pushed, forming the wings and the bended shape. The ionization pressure might still be effective towards the low-density northern part of RCW 120, where a champagne flow is observed and toward the south center where bended structured can be observed on *Herschel* observations.

Because $P_{clump} \sim P_{ion}$, Torii et al. (2015) concluded that the ionization pressure cannot create the cavity, making the C&C scenario inconsistent. However, the expansion of the H II region might have compressed the layer and stopped when $P_{clump} \sim P_{ion}$. This is consistent with the fact that we barely detect any motion of the ring, with an expansion velocity of between 1.2 and 2.3 km s$^{-1}$ (Anderson et al. 2015).

## 4. Discussion

### 4.1. Dynamics of the region

Both regions contain protostars, which are either at the beginning of their evolution (region A) or are more advanced YSOs (region B), at different projected distances from the ionizing star; these are therefore differently impacted by the UV radiation. The Mach numbers of regions A and B are high compared to the literature, indicating that turbulence is significant in these regions. In region A, this turbulence can be explained by the impact of UV radiation on the clump, by the ongoing star formation, and by the outflow toward the massive ~300 $M_\odot$ *Herschel* source. This can explain the mass of the fragments at 0.01 pc scale (Figueira et al. 2018), which is in disagreement with the thermal Jeans mechanism. In region B, the turbulence is less important and could be explained by the lower impact of stellar feedback from low-mass stars. Indeed, the spectral profile is not broad and no tracers of shock were detected using the MALT90 survey. In addition, the clump being farther away, the impact of UV radiation should be less significant.

We tried to understand the impact of UV radiation on the abundance of $^{13}$CO and C$^{18}$O, and on the photodissociation of C$^{18}$O. Using the mass derived from the *Herschel* column density map, the abundances of $^{13}$CO and C$^{18}$O are found to be lower compared to the general ISM values ($2.7 \times 10^{-6}$ and $1.7 \times 10^{-7}$, respectively, Goldsmith et al. 1997; Magnani et al. 1988; Pineda et al. 2008). However, several sources of bias have to be taken into account before drawing any conclusions from these values.

Firstly, the N(H$_2$) mass differs from the one estimated by Deharveng et al. (2009) by a factor of three at most, and therefore the abundance would increase by the same factor. Secondly, $^{13}$CO being moderately thick toward the densest parts, the derived N($^{13}$CO) represents a lower limit. Accounting for this mass uncertainty on C$^{18}$O does not rule out a possible photodissociation.

The average ratio of $^{13}$CO to C$^{18}$O is equal to 4.6 and 7.4 for regions A and B, respectively. These values are close to the value of 5.5 for the Solar System and far from the high ratio observed towards Orion-A of 16.5 and the maximum of 33 (Shimajiri et al. 2014). By looking at the ratio maps, we observed that the value for this latter ratio is lower towards the densest part of the region and higher toward the edges. Unfortunately, as noted by Shimajiri et al. (2014), this ratio is affected by the beam filling factor which could be as low as 0.4 as well as being nonuniform over the area due to the different structures observed (Paron et al. 2018). The resolution of our observations does not allow us to come to a conclusion as to the dissociation of C$^{18}$O towards the PDR of RCW 120.

## 4.2. Induced star formation toward RCW 120

### 4.2.1. Collect and collapse mechanism

The interplay between the ionizing radiation from massive stars and the turbulent medium was analyzed by Tremblin et al. (2012) using hydrodynamical simulations. These latter authors showed that the probability density function (PDF) of the gas can be used to trace the unperturbed and shocked gas. The PDF of the highest density clump (region A) is well fitted by a power law, showing the relation between the ionization pressure and the compression of this clump (Tremblin et al. 2014). Studies by Thompson et al. (2012) and Minier et al. (2013) also indicate that this clump is likely to be triggered by the H II region. This compression would locally increase the density and lead to the gravitational collapse of the layer. However, the mechanism responsible for the formation of this clump, where most the massive cores are found, remains unclear.

As seen in Fig. 1, this clump does not seem to be pre-existent as the interface between the PDR and the H II region is not distorted. Therefore, the spatial distribution of the dust and gas in this region would be visually in agreement with the C&C mechanism. We note that the CCC model would give the same ring-like dust distribution but star formation would not be the result of any compression as the ring would have formed before emission of UV radiation.

To better understand if the C&C process could be at work, we compared the dynamical age of the HII region, $t_{\mathrm{dyn}}$, to the time needed for the layer to fragment, $t_{\mathrm{frag}}$. Such comparisons have been performed in the past: towards S 233 (Ladeyschikov et al. 2015) and S 24 (Cappa et al. 2016), the C&C mechanism does not seem to be possible while toward Sh2-39 (Duronea et al. 2017), Sh2-104 (Xu et al. 2017), Sh2-212 (Deharveng et al. 2008), Gum 31 (Duronea et al. 2015), and Sh 217 (Brand et al. 2011), the C&C model appears to be plausible.

In this work, we estimated $t_{\mathrm{dyn}}$ using the model of Tremblin et al. (2014). We use the same set of equations as in their work, from Martín-Hernández et al. (2005):

$$N_{\mathrm{LyC}} = \left(\frac{7.603 \times 10^{46}\,\mathrm{s}^{-1}}{b(\nu, T_e)}\right)\left(\frac{S_\nu}{\mathrm{Jy}}\right)\left(\frac{T_e}{10^4\,\mathrm{K}}\right)^{-0.33}\left(\frac{D}{\mathrm{kpc}}\right)^2, \quad (7)$$

$$b(\nu, T_e) = 1 + 0.3195\log\left(\frac{T_e}{10^4\,\mathrm{K}}\right) - 0.2130\log\left(\frac{\nu}{\mathrm{GHz}}\right). \quad (8)$$

The thermal radio-continuum emission of RCW 120 is equal to 5.81 and 8.52 Jy at 8.35 and 14.35 GHz, respectively (Langston et al. 2000). The value of $\log(N_{\mathrm{LyC}})$ is found to be 48.14 $\mathrm{s}^{-1}$. The radius of the bubble is taken to be 1.8 pc (277″ at 1.34 kpc).

The last parameter needed is the initial density of the medium $n_0$. We estimated $n_0$ by assuming that all the mass was initially gathered in a sphere of ~1.8 pc radius. The mass of RCW 120 at 870 $\mu$m, assuming $T = 20$ K, is ~2000 $M_\odot$ (Deharveng et al. 2009). However, observations with APEX-LABOCA suffer from loss of large-scale emission. Using the maps combined with *Planck* data (Csengeri et al. 2016) to correct for this emission loss, the mass of RCW 120 (contour of 0.6 Jy beam$^{-1}$, $T = 20$ K) increases to 2600 $M_\odot$. Using the column density map of RCW 120 (Figueira et al. 2017), the mass of the layer is 6000 $M_\odot$ and increases to $10^4$ $M_\odot$ if we consider the whole region.

The mass from LABOCA+*Planck* (lower limit) and from N(H$_2$) (upper limit) found give an initial density of $1.85 \times 10^3$ and $7.13 \times 10^3$ cm$^{-3}$, respectively. From the statistical study of
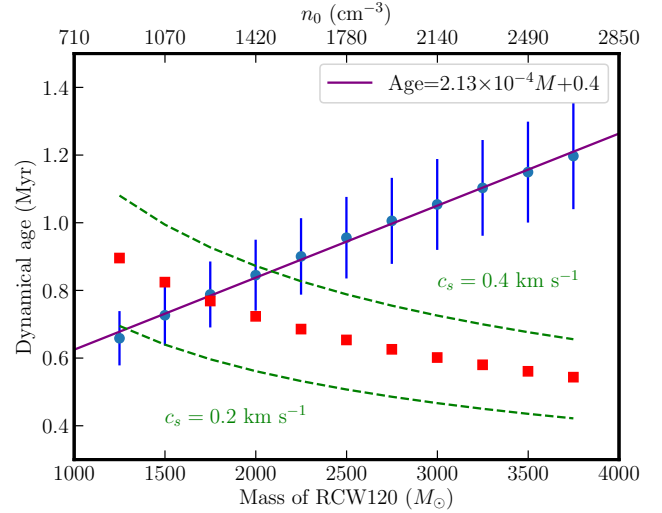


**Fig. 11.** Dynamical age as a function of the mass (bottom axis) and as a function of initial density (top axis) of RCW 120 (blue dot), with the uncertainty associated to each of them (blue bars) and the linear fit (purple line). The fragmentation timescale following the model of Whitworth et al. (1994) is plotted for $N_{\mathrm{LyC}} = 10^{48}$ s$^{-1}$ and $c_s = 0.3$ (red squares), and for $c_s = 0.2, 0.4$ km s$^{-1}$ (green dashed lines).

**Table 4.** Age of RCW 120 in the literature.

| Reference | $n_0$ ($\times 10^3$ cm$^{-3}$) | Age (Myr) |
|---|---|---|
| This work | 1.9−7.1 | 0.96 ± 0.25 |
| | | 0.75 ± 0.13 |
| Martins et al. (2010) [a] | | <5 |
| Arthur et al. (2011) | 1 | 0.2 |
| Marsh & Whitworth (2019) | 1−3 | 0.23−0.42 |
| Zavagno et al. (2007) | 3 | 0.4 |
| Pavlyuchenkov et al. (2013) | 3−10 | 0.17−0.32 |
| Akimkin et al. (2017) | 1 | 0.26−0.63 |

**Notes.** [a] In Martins et al. (2010), the estimation is obtained using isochrones.

Palmeirim et al. (2017) with Hi-GAL (Molinari et al. 2010), H II regions in the Galactic plane have density ranging from ~10 to ~2300 cm$^{-3}$ and most of the simulations take initial density between 1000 and 3000 cm$^{-3}$ (Arthur et al. 2011; Walch et al. 2015; Mackey et al. 2016; Marsh & Whitworth 2019). Therefore, the initial density of $7.13 \times 10^3$ cm$^{-3}$ seems too high compared to the usual values found toward H II regions.

In the model of Tremblin et al. (2014), the input density is given by the average density at 1 pc. To compute the dynamical age, we used the nearest grid values to the estimations (8000 K, 1.8 pc and $10^{48}$ s$^{-1}$). Uncertainties were estimated using the grid values below and above the estimations. The results are plotted on Fig. 11. The dynamical age as well as those taken from other works are listed in Table 4. At the lowest density ($1.9 \times 10^3$ cm$^{-3}$), the dynamical age of RCW 120 can be two to four times higher than the values usually found in the literature.

Previously, we mentioned that part of $N_{\mathrm{LyC}}$ could be absorbed by the dust, and this fraction can range from 25 to 50% (Inoue 2001). Therefore, $N_{\mathrm{LyC}} = (1 - f_0)N^*_{\mathrm{LyC}}$, where $f_0$ represents the absorption by dust, is a lower limit of the true $N^*_{\mathrm{LyC}}$. Following the calibration of O stars from Martins et al. (2005),

$N_{\text{LyC}} = 10^{48.29}$ s$^{-1}$ for a O8V star. Compared to the previous estimation, up to 30% of the ionizing photons are absorbed by the dust. Taking a flux of $10^{48.5}$ in the model, $t_{\text{dyn}}$ decreases to $0.75 \pm 0.13$ Myr.

Having an estimation of $t_{\text{dyn}}$ allows a comparison with $t_{\text{frag}}$, the time needed for the layer to start fragmenting under the C&C mechanism, using the analytical expression of Whitworth et al. (1994):

$$t_{\text{frag}} \sim 1.56 \text{ Myr} \left( \frac{c_s}{0.2 \text{ km s}^{-1}} \right)^{\frac{7}{11}} \left( \frac{N_{\text{LyC}}}{10^{49} \text{ s}^{-1}} \right)^{\frac{-1}{11}} \left( \frac{n_0}{10^2 \text{ cm}^{-3}} \right)^{\frac{-5}{11}} . \tag{9}$$

We note that the normalization constants used in Whitworth et al. (1994) are extreme values, chosen to minimize the mass of the fragments. For the density normalization, a most realistic value proposed in the same work is 100 cm$^{-1}$, used in Eq. (9), leading to a factor of 0.35 for $t_{\text{frag}}$. Such $n_0$ has been used by Palmeirim et al. (2017) for instance.

On first approximation, $c_s$ depends on the temperature of the shell which is 28.3 K for region A based on CO observations, giving $c_s = 0.3$ km s$^{-1}$. However, this is a lower limit as turbulence and sub-Lyman radiation leaking through the PDR could enhance it. $N_{\text{LyC}}$ does not have a lot of weight with respect to $t_{\text{frag}}$, leading to a change of $\pm 0.3$ Myr for a difference of one order of magnitude. An increase will lower $t_{\text{frag}}$ as the column density threshold necessary for fragmentation would be reached faster. The dependence of $t_{\text{frag}}$ with respect to the mass of RCW 120 (equivalently, $n_0$) is plotted on Fig. 11. As for $N_{\text{LyC}}$, a higher $n_0$ decreases $t_{\text{frag}}$ since the column density threshold is reached faster. We also computed $t_{\text{frag}}$ using $c_s = 0.2-0.4$ to quantify the difference.

For a mass of 2600 $M_\odot$, $t_{\text{frag}} = 0.5-0.7-0.8$ Myr (see Fig. 11). Because $t_{\text{dyn}} < t_{\text{frag}}$, the C&C mechanism seems be the most likely explanation for the fragmentation of the surrounding shell around the ionizing star. Simulations of Akimkin et al. (2017) and Zavagno et al. (2007) are also favorable to the C&C mechanism at a density of $3 \times 10^3$ cm$^{-3}$. However, Kirsanova et al. (2014) found the C&C mechanism to be unlikely unless the density reaches $7 \times 10^3$ cm$^{-3}$. This difference can explained by the choice of normalization for $n_0$. Indeed, the dynamical age in their work at ~3000 cm$^{-3}$ is 2 Myr, which would be reduced to 0.7 Myr with a normalization of 100 cm$^{-3}$. The comparison of $t_{\text{dyn}}$ and $t_{\text{frag}}$ in this work would support the idea of triggering but, as we see in Table 4, the age of RCW 120 in the literature might be as low as 0.17 Myr, which would make the C&C inconsistent.

Dale et al. (2009) showed that, without pressure confinement, the thickness of the layer increases with time, as observed towards H II bubbles (Churchwell et al. 2007). However, the simulations do not agree with the thin shell approximation used in the analytical model. Additionally, the magnetic field should also be taken into account (Fukuda & Hanawa 2000).

Therefore, conclusions from this model, even if it supports the idea of triggered star formation, must be taken with caution. Detailed analysis of the interplay between the H II region and the PDR (Tremblin et al. 2014; Figueira et al. 2018; Zavagno et al. 2020) might be a better indicator but are also not exempt from some uncertainties (Dale et al. 2015) regarding induced star formation.

### 4.2.2. Radiation-driven implosion process toward region B

Several works have studied the impact of the photoionization pressure on the induction of star formation in pre-existing

clumps. The study of Urquhart et al. (2009), using a sample of 45 clouds from the SFO catalog (Sugitani et al. 1991; Sugitani & Ogura 1994), allowed the authors to understand the difference in terms of physical properties between clouds where RDI is happening and where it is unlikely. For instance, an IBL through hydrogen recombination and a PDR through PAH emission at 8 $\mu$m should be observed. As UV radiation should heat the cloud, $T_{\text{ex}}^{12}$ should be higher, and higher than $T_{\text{ex}}^{18}$. Moreover, some clouds triggered by the RDI mechanism show multiple components in CO, indicative of shocked and/or moving gas. As the ionization front propagates into the clump, sequential star formation might be observed. Additionally, RDI is thought to be efficient, leading in priority to a high-mass star or a cluster of intermediate-mass stars (Sugitani et al. 1991; Morgan et al. 2008) toward the center of the clump (Kessel-Deynet & Burkert 2003). Estimations of the turbulence from NH$_3$ (Morgan et al. 2010) showed a clear bimodality with a higher turbulence in the triggered sample of BRCs.

Observations from SHS (SuperCOSMOS H$\alpha$ Survey, Parker et al. 2005) show that the H$\alpha$ emission stops where the 8 $\mu$m emission is located but no clear IBL is observed, despite a high $n_e$. On the other hand, the curved rim is clearly seen at 8 $\mu$m, tracing the PDR and indicating a strong interaction between the clump and the UV radiation. It should be noted that, as Herbig Ae/Be stars may be present in region B (source 24 and 28), the PAH present around them could be partially attributable to their own FUV radiation (Seok & Li 2017).

As discussed above (see Table 2), $T_{\text{ex}}^{12}$ is found to be ~21 K on average which is in agreement with Urquhart et al. (2009) for the sample of triggered BRCs. The values of $T_{\text{ex}}^{18}$ are found to be quite similar to $T_{\text{ex}}^{12}$ which might be explained by evolved YSOs inside region B (Deharveng et al. 2009), heating the clump.

Several CO observations pointed out that multiple components, representing the dynamics, can be observed towards triggered BRCs. Different components ($-12$, $-10$ and $-1$ km s$^{-1}$) are observed toward region B (Fig. A.1) but likely correspond to cloud emission on the line of sight (see Fig. 11 of Anderson et al. 2015). We note that the absence of multiple components in a CO spectrum does not mean that the RDI process should be discarded. The sample of southern BRCs studied by Urquhart et al. (2009) was classified between spontaneous and triggered candidates based on the association with a PDR or an IBL. SFOs 51 and 59, which are part of the spontaneous sample, show multiple components, but SFOs 64 and 65 show only a single component while being considered as triggered candidates.

Based on the classification of YSOs in Deharveng et al. (2009), sources in region B are Class I-II (Deharveng et al. 2009) and therefore star formation is likely to be coeval in that clump. As the UV radiation interacts with the edge and propagates inside the clump, sequential star formation or similar YSOs at the same location can be expected. From the analysis of the $L_{\text{bol}} - M_{\text{env}}$ diagram in Figueira et al. (2017), we also note that they are the most evolved YSOs in RCW 120 and were probably formed before the majority of the sources found in the PDR. This strengthens the idea that the clump in region B was pre-existing and star formation begins there when the rest of layer was still assembling.

The SFE is difficult to estimate since the stellar masses are unknown. However, we can estimate the core formation efficiency (CFE) based on the mass of the cores and dust. Following Figueira et al. (2017), the total mass of the cores is 23 $M_\odot$ and the mass of the clump is between 90 and 200 $M_\odot$. The CFE varies between 12 and 26% and since part of the envelope will be swept away during the formation of the stars, the final SFE will

be lower than these values. Toward the Cepheus B population, Getman et al. (2009) found that RDI is likely to have triggered star formation and that the SFE is between 35 and 55%, well above the values found for region B. In the case of RCW 120, the H II region interaction might have formed stars in a shorter time but no high SFE is observed.

We compared our results with the RDI simulations developed by Miao et al. (2009), and in particular cloud A of the first set ($n_0 = 2672$ cm$^{-3}$, $R = 0.5$ pc). At the end of the simulation, the pressure of the clump is $\sim 10^6$ K cm$^{-3}$. A core is formed with a density of $10^5$ cm$^{-3}$, a temperature of 28 K, and a mass of 15 $M_\odot$ and is found up to 0.3 pc from the surface layer. Compared to region B, the pressure of the cloud is lower but may be due to the difference in initial density. Several cores have formed at the clump surface but we often observed multiple stars forming instead of one unique core at the top of the cloud if the BRC is not symmetrical (Sicilia-Aguilar et al. 2014). Regarding the CFE, it rises to 38% and is well above the value of 12 to 26% estimated above.

Finally, the formation of an A-type morphology for the BRC and the collapse of the core takes about 0.4 Myr. This is in agreement, because the dynamical age of RCW 120 is above this value. During the remaining 0.5 Myr after the formation of the BRC, the cores evolved into Class I-II YSOs or stars and the ionization pressure increased the density of the clump, leading to a higher clump pressure. As already found by Lefloch & Lazareff (1994), Miao et al. (2009) showed that clouds located closer to the ionizing source will evolve to a type-A BRC. This is in agreement with the slightly curved clump of region B.

Compared to the simulations of Kinnear et al. (2015), the time needed for the formation of a BRC is much lower ($\sim 0.1$ Myr). However in that case, the total core mass produced is lower ($\sim 1.5$ $M_\odot$) and the resulting CFE is around 5%.

Simulations of Haworth et al. (2013) show a curved morphology of the CO distribution after the interaction with the H II region. This is observed at 8 $\mu$m but not in CO as the resolution might be too low ($\sim 18.2''$). Depending on the strength of the ionizing flux and the viewing angle, the CO profiles can have multiple components, representing the dynamics of the clump. As we stressed before, CO profiles of triggered BRCs can show multiple components (Urquhart et al. 2009; Morgan et al. 2009) but this is not a requirement as it can depend on the viewing angle and ionizing flux strength.

The variation of the line profile symmetry parameter $\delta$ (Mardones et al. 1997) was also studied as a function of viewing angle. Considering the profile of $^{12}$CO and C$^{18}$O, we found $\delta \sim 0.2$, corresponding to an angle of $-20°$ which indicates that the ionizing star should be in front of the dusty ring. This is in agreement with the PAH emission at 8 $\mu$m which appears face on while it would be unobservable if UV emission was coming from behind, as stated by Urquhart et al. (2009).

## 5. Conclusions

Here, we analyze the $^{12}$CO, $^{13}$CO, and C$^{18}$O in the $J = 3-2$ molecular transition toward two subregions located in the PDR of the Galactic H II region RCW 120. The region A corresponds to a high-mass clump where young high-mass cores were detected with *Herschel* and ALMA while evolved low-mass YSOs were found in region B. Derivation of the velocity dispersion maps shows an increase in both regions where star formation is observed and, assuming LTE, $T_{ex}$ is also found to increase toward the same locations. The estimated Mach number for both regions shows the supersonic motions inside the

PDR due to the impact of FUV and feedback from star formation occurring there. The properties of the outflow toward the massive core of region A, traced by molecular transition from MALT90, are in good agreement with MSF regions from the literature.

We discuss the star formation with respect to the C&C mechanism and find that the time needed for the layer to fragment is equivalent to the dynamical age of RCW 120. It also appears clear from other studies that the H II region compressed the layer.

Toward region B, no IBL is observed compared to what is predicted by the high electron density value but PAH emission is observed. Additionally, the radio emission engulfs the clump in region B and the 8 $\mu$m emission shows wings and the BRC shows an A-type morphology. From simulations based on the RDI mechanism, the time needed for the ionization to form stars is in agreement with the dynamical age of the H II region. The higher pressure of the clump compared to the ionization pressure shows that the compression of this clump stopped, in agreement with the low expansion velocity of the region. Therefore, region B appears to be a good candidate for the RDI mechanism.

## References

Akimkin, V. V., Kirsanova, M. S., Pavlyuchenkov, Y. N., & Wiebe, D. S. 2017, MNRAS, 469, 630
Anderson, L. D., Zavagno, A., Deharveng, L., et al. 2012, A&A, 542, A10
Anderson, L. D., Bania, T. M., Balser, D. S., et al. 2014, ApJS, 212, 1
Anderson, L. D., Deharveng, L., Zavagno, A., et al. 2015, ApJ, 800, 101
Arce, H. G., Shepherd, D., Gueth, F., et al. 2007, in Protostars and Planets V, eds. B. Reipurth, D. Jewitt, & K. Keil (Tucson: University of Arizona Press), 245
Arthur, S. J., Henney, W. J., Mellema, G., de Colle, F., & Vázquez-Semadeni, E. 2011, MNRAS, 414, 1747
Balser, D. S., Rood, R. T., Bania, T. M., & Anderson, L. D. 2011, ApJ, 738, 27
Beaumont, C. N., & Williams, J. P. 2010, ApJ, 709, 791
Bertoldi, F. 1989, ApJ, 346, 735
Bisbas, T. G., Wünsch, R., Whitworth, A. P., Hubber, D. A., & Walch, S. 2011, ApJ, 736, 142
Blaauw, A. 1964, ARA&A, 2, 213
Brand, J., Massi, F., Zavagno, A., Deharveng, L., & Lefloch, B. 2011, A&A, 527, A62
Cappa, C. E., Duronea, N., Firpo, V., et al. 2016, A&A, 585, A30
Caswell, J. L. 2013, IAU Symp., 292, 79
Caswell, J. L., & Haynes, R. F. 1987, A&A, 171, 261
Churchwell, E., Watson, D. F., Povich, M. S., et al. 2007, ApJ, 670, 428
Coffey, D., Bacciotti, F., & Podio, L. 2008, ApJ, 689, 1112
Csengeri, T., Weiss, A., Wyrowski, F., et al. 2016, A&A, 585, A104
Dale, J. E. 2017, MNRAS, 467, 1067
Dale, J. E., & Bonnell, I. 2011, MNRAS, 414, 321
Dale, J. E., Ercolano, B., & Bonnell, I. A. 2012, MNRAS, 427, 2852
Dale, J. E., Ercolano, B., & Bonnell, I. A. 2013, MNRAS, 431, 1062
Dale, J. E., Haworth, T. J., & Bressert, E. 2015, MNRAS, 450, 1199
Dale, J. E., Wünsch, R., Whitworth, A., & Palouš, J. 2009, MNRAS, 398, 1537
de Villiers, H. M., Chrysostomou, A., Thompson, M. A., et al. 2014, MNRAS, 444, 566
Deharveng, L., Lefloch, B., Kurtz, S., et al. 2008, A&A, 482, 585
Deharveng, L., Zavagno, A., Schuller, F., et al. 2009, A&A, 496, 177
Deharveng, L., Schuller, F., Anderson, L. D., et al. 2010, A&A, 523, A6
Duronea, N. U., Vasquez, J., Gómez, L., et al. 2015, A&A, 582, A2
Duronea, N. U., Cappa, C. E., Bronfman, L., et al. 2017, A&A, 606, A8
Elmegreen, B. G., & Lada, C. J. 1977, ApJ, 214, 725
Federrath, C., & Klessen, R. S. 2012, ApJ, 761, 156
Figueira, M., Zavagno, A., Deharveng, L., et al. 2017, A&A, 600, A93
Figueira, M., Bronfman, L., Zavagno, A., et al. 2018, A&A, 616, L10
Fukuda, N., & Hanawa, T. 2000, ApJ, 533, 911

Fukuda, N., Miao, J., Sugitani, K., et al. 2013, ApJ, 773, 132
Geen, S., Rosdahl, J., Blaizot, J., Devriendt, J., & Slyz, A. 2015, MNRAS, 448, 3248
Geen, S., Hennebelle, P., Tremblin, P., & Rosdahl, J. 2016, MNRAS, 463, 3129
Geen, S., Pellegrini, E., Bieri, R., & Klessen, R. 2019, MNRAS, 492, 915
Getman, K. V., Feigelson, E. D., Luhman, K. L., et al. 2009, ApJ, 699, 1454
Goldsmith, P. F., Bergin, E. A., & Lis, D. C. 1997, IAU Symp., 170, 113
González Lobos, V., & Stutz, A. M. 2019, MNRAS, 489, 4771
Güsten, R., Nyman, L. Å., Schilke, P., et al. 2006, A&A, 454, L13
Haworth, T. J., Harries, T. J., Acreman, D. M., & Rundle, D. A. 2013, MNRAS, 431, 3470
Inoue, A. K. 2001, AJ, 122, 1788
Jijina, J., & Adams, F. C. 1996, ApJ, 462, 874
Kendrew, S., Simpson, R., Bressert, E., et al. 2012, ApJ, 755, 71
Kendrew, S., Beuther, H., Simpson, R., et al. 2016, ApJ, 825, 142
Kessel-Deynet, O., & Burkert, A. 2003, MNRAS, 338, 545
Kinnear, T. M., Miao, J., White, G. J., Sugitani, K., & Goodwin, S. 2015, MNRAS, 450, 1017
Kirsanova, M. S., Pavlyuchenkov, Y. N., Wiebe, D. S., et al. 2019, MNRAS, 488, 5641
Kirsanova, M. S., Wiebe, D. S., Sobolev, A. M., Henkel, C., & Tsivilev, A. P. 2014, MNRAS, 437, 1593
Kohno, M., Tachihara, K., Fujita, S., et al. 2018, PASJ, 126 https://academic.oup.com/pasj/article/doi/10.1093/pasj/psy109/5168161?searchresult=1
Krumholz, M. R., Bate, M. R., Arce, H. G., et al. 2014, Protostars and Planets VI (Tucson: University of Arizona Press), 243
Ladeyschikov, D. A., Sobolev, A. M., Parfenov, S. Y., Alexeeva, S. A., & Bieging, J. H. 2015, MNRAS, 452, 2306
Langston, G., Minter, A., D'Addario, L., et al. 2000, AJ, 119, 2801
Lefloch, B., & Lazareff, B. 1994, A&A, 289, 559
Lefloch, B., Lazareff, B., & Castets, A. 1997, A&A, 324, 249
Mackey, J., Haworth, T. J., Gvaramadze, V. V., et al. 2016, A&A, 586, A114
Magnani, L., Blitz, L., & Wouterloot, J. G. A. 1988, ApJ, 326, 909
Mardones, D., Myers, P. C., Tafalla, M., et al. 1997, ApJ, 489, 719
Marsh, K. A., & Whitworth, A. P. 2019, MNRAS, 483, 352
Martín-Hernández, N. L., Vermeij, R., & van der Hulst, J. M. 2005, A&A, 433, 205
Martins, F., Schaerer, D., & Hillier, D. J. 2005, A&A, 436, 1049
Martins, F., Pomarès, M., Deharveng, L., Zavagno, A., & Bouret, J. C. 2010, A&A, 510, A32
Maud, L. T., Moore, T. J. T., Lumsden, S. L., et al. 2015, MNRAS, 453, 645
McLeod, A. F., Reiter, M., Kuiper, R., Klaassen, P. D., & Evans, C. J. 2018, Nature, 554, 334
Miao, J., White, G. J., Nelson, R., Thompson, M., & Morgan, L. 2006, MNRAS, 369, 143
Miao, J., White, G. J., Thompson, M. A., & Nelson, R. P. 2009, ApJ, 692, 382
Minier, V., Tremblin, P., Hill, T., et al. 2013, A&A, 550, A50
Molinari, S., Swinyard, B., Bally, J., et al. 2010, PASP, 122, 314
Morgan, L. K., Thompson, M. A., Urquhart, J. S., & White, G. J. 2008, A&A, 477, 557
Morgan, L. K., Urquhart, J. S., & Thompson, M. A. 2009, MNRAS, 400, 1726
Morgan, L. K., Figura, C. C., Urquhart, J. S., & Thompson, M. A. 2010, MNRAS, 408, 157
Murphy, T., Mauch, T., Green, A., et al. 2007, MNRAS, 382, 382

Orkisz, J. H., Pety, J., Gerin, M., et al. 2017, A&A, 599, A99
Palmeirim, P., Zavagno, A., Elia, D., et al. 2017, A&A, 605, A35
Parker, Q. A., Phillipps, S., Pierce, M. J., et al. 2005, MNRAS, 362, 689
Paron, S., Areal, M. B., & Ortega, M. E. 2018, A&A, 617, A14
Pavlyuchenkov, Y. N., Kirsanova, M. S., & Wiebe, D. S. 2013, Astron. Rep., 57, 573
Pineda, J. E., Caselli, P., & Goodman, A. A. 2008, ApJ, 679, 481
Preibisch, T., & Zinnecker, H. 2007, IAU Symp., 237, 270
Rahner, D., Pellegrini, E. W., Glover, S. C. O., & Klessen, R. S. 2019, MNRAS, 483, 2547
Rohlfs, K., & Wilson, T. L. 1996, Tools of Radio Astronomy (Berlin: Springer), 127
Russeil, D. 2003, A&A, 397, 133
Russeil, D., Figueira, M., Zavagno, A., et al. 2019, A&A, 625, A134
Schilke, P. 2015, EAS Pub. Ser., 75, 227
Seok, J. Y., & Li, A. 2017, ApJ, 835, 291
Shimajiri, Y., Kitamura, Y., Saito, M., et al. 2014, A&A, 564, A68
Sicilia-Aguilar, A., Roccatagliata, V., Getman, K., et al. 2014, A&A, 562, A131
Spitzer, L. 1978, Physical processes in the interstellar medium (Hoboken: John Wiley & Sons)
Strömgren, B. 1939, ApJ, 89, 526
Sugitani, K., & Ogura, K. 1994, ApJS, 92, 163
Sugitani, K., Fukui, Y., & Ogura, K. 1991, ApJS, 77, 59
Takekoshi, T., Fujita, S., Nishimura, A., et al. 2019, ApJ, 883, 156
Thompson, M. A., Urquhart, J. S., & White, G. J. 2004, A&A, 415, 627
Thompson, M. A., Urquhart, J. S., Moore, T. J. T., & Morgan, L. K. 2012, MNRAS, 421, 408
Tigé, J., Motte, F., Russeil, D., et al. 2017, A&A, 602, A77
Torii, K., Hasegawa, K., Hattori, Y., et al. 2015, ApJ, 806, 7
Traficante, A., Fuller, G. A., Smith, R. J., et al. 2018, MNRAS, 473, 4975
Tremblin, P., Audit, E., Minier, V., Schmidt, W., & Schneider, N. 2012, A&A, 546, A33
Tremblin, P., Schneider, N., Minier, V., et al. 2014, A&A, 564, A106
Urquhart, J. S., Thompson, M. A., Morgan, L. K., & White, G. J. 2004, A&A, 428, 723
Urquhart, J. S., Morgan, L. K., & Thompson, M. A. 2009, A&A, 497, 789
van der Walt, D. J., Sobolev, A. M., & Butner, H. 2007, A&A, 464, 1015
Vassilev, V., Meledin, D., Lapkin, I., et al. 2008, A&A, 490, 1157
Vazzano, M. M., Cappa, C. E., Rubio, M., et al. 2019, Rev. Mex. Astron. Astrofis., 55, 289
Walch, S., Whitworth, A. P., Bisbas, T. G., Hubber, D. A., & Wünsch, R. 2015, MNRAS, 452, 2794
Ward-Thompson, D., Nutter, D., Bontemps, S., Whitworth, A., & Attwood, R. 2006, MNRAS, 369, 1201
Whitworth, A. P., Bhattal, A. S., Chapman, S. J., Disney, M. J., & Turner, J. A. 1994, MNRAS, 268, 291
Wolfire, M. G., & Cassinelli, J. P. 1987, ApJ, 319, 850
Wu, B., Tan, J. C., Nakamura, F., Christie, D., & Li, Q. 2018, PASJ, 70, S57
Xu, J.-L., Xu, Y., Yu, N., et al. 2017, ApJ, 849, 140
Xu, J.-L., Zavagno, A., Yu, N., et al. 2019, A&A, 627, A27
Yang, A. Y., Thompson, M. A., Urquhart, J. S., & Tian, W. W. 2018, ApJS, 235, 3
Zavagno, A., Pomarès, M., Deharveng, L., et al. 2007, A&A, 472, 835
Zavagno, A., Russeil, D., Motte, F., et al. 2010, A&A, 518, L81
Zavagno, A., André, P., Schuller, F., et al. 2020, A&A, 638, A7

## Appendix A: Pixel spectra
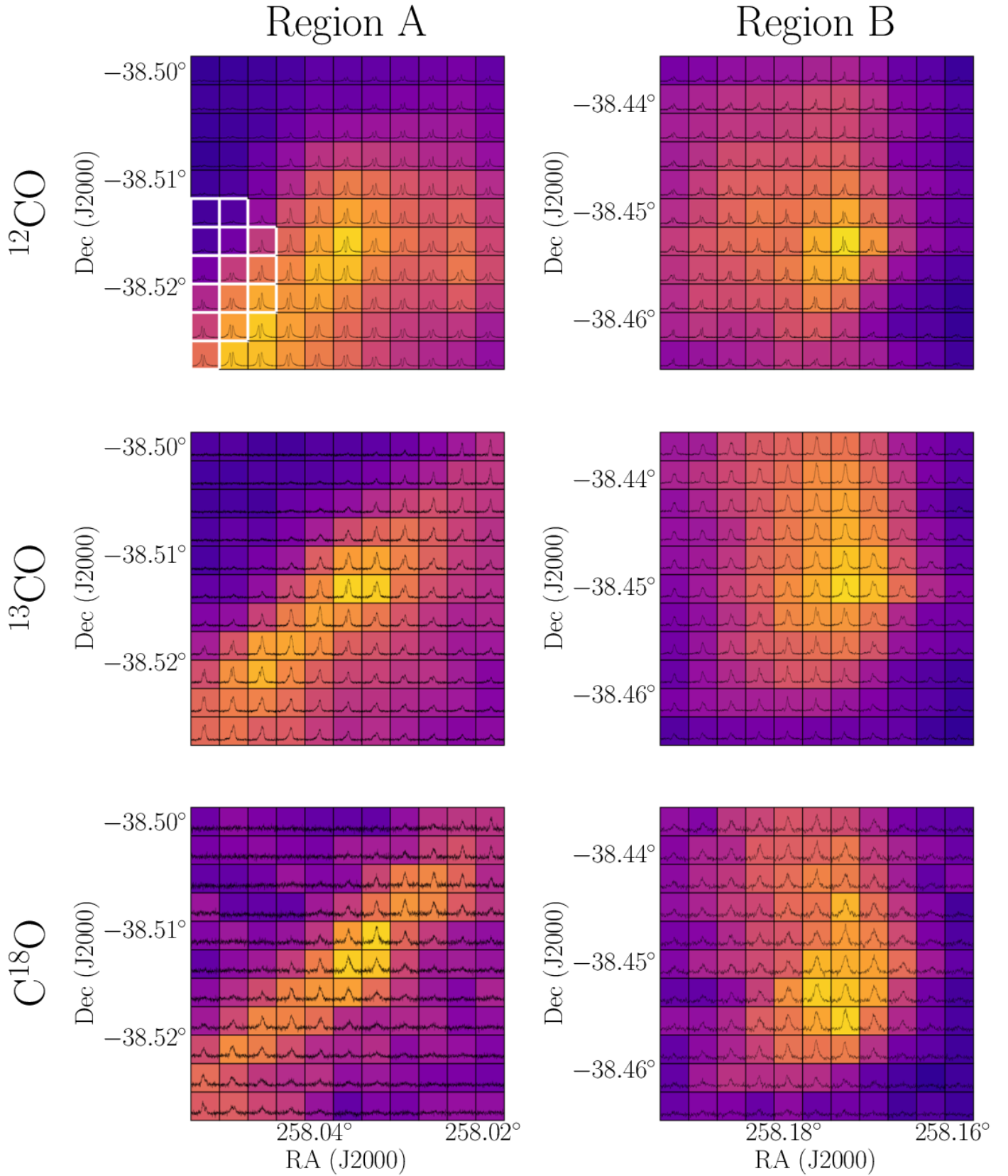


**Fig. A.1.** $^{12}$CO, $^{13}$CO, and C$^{18}$O spectra at each pixel of the maps toward regions A (*first column*) and B (*second column*). Pixel spectra have the same axis range within the same map but differ from region to region and from one isotopolog to another. Pixels with white edges indicate where a second component is seen at $-15$ km s$^{-1}$.